Arabian Journal of Chemistry (2020) 13, 4324–4340

King Saud University

Arabian Journal of Chemistry

www.ksu.edu.sa
www.sciencedirect.com

ORIGINAL ARTICLE

Magnetically separable $ZnO/ZnFe_2O_4$ and $ZnO/CoFe_2O_4$ photocatalysts supported onto nitrogen doped graphene for photocatalytic degradation of toxic dyes

Naresh Chandel [a], Kirti Sharma [a], Anita Sudhaik [a], Pankaj Raizada [a,b], Ahmad Hosseini-Bandegharaei [c,d], Vijay Kumar Thakur [e], Pardeep Singh [a,b,*]

[a] *School of Chemistry, Faculty of Basic Sciences, Shoolini University, Solan, Himachal Pradesh 173212, India*
[b] *Himalayan Centre for Excellence in Nanotechnology, Shoolini University, Solan, HP 173229, India*
[c] *Department of Environmental Health Engineering, Faculty of Health, Sabzevar University of Medical Sciences, Sabzevar, Iran*
[d] *Department of Engineering, Kashmar Branch, Islamic Azad University, PO Box 161, Kashmar, Iran*
[e] *Enhanced Composites and Structures Center, School of Aerospace, Transport and Manufacturing, Cranfield University, Bedfordshire MK43 0AL, UK*

Received 17 May 2019; accepted 12 August 2019
Available online 23 August 2019

KEYWORDS

$ZnFe_2O_4$;
$CoFe_2O_4$;
Nitrogen doped graphene;
Supported photocatalysis
Magnetic separation;
Dye mineralization;
Recycle efficiency

Abstract Advanced oxidation processes (AOPs) counting heterogeneous photocatalysis has confirmed as one of the preeminent method for waste water remediation. In the present work, we have successfully fabricated novel visible-light-driven nitrogen-doped graphene (NG) supported magnetic $ZnO/ZnFe_2O_4$ (ZnO/ZF/NG) and $ZnO/CoFe_2O_4$ (ZnO/CF/NG) nanocomposites. ZnO synthesized *via* direct precipitation method. Hydrothermal method was used for the preparation of nitrogen-doped graphene supported magnetic ZnO/ZF ($ZnO/ZnFe_2O_4$) and ZnO/CF ($ZnO/CoFe_2O_4$) nanocomposites. The procured materials were scrutinized by assorted characterizations to acquire information on their chemical composition, crystalline structure and photosensitive properties. The absorption and photocatalytic performance of photocatalysts were studied *via* UV–Visible spectra. Photodegradation performance of the synthesized nanocomposites was estimated toward mineralization of methyl orange (MO) and malachite green (MG) dyes in aqueous solution. The high surface area of ZnO/ZF/NG and ZnO/CF/NG was suitable for adsorptive removal of MO and MG dyes. The photodegradation performance of heterojunction photocatalysts was superior to bare photocatalyst in 140 min under visible-light irradiation. Spectrophotometer, GC–MS

* Corresponding author at: School of Chemistry, Faculty of Basic Sciences, Shoolini University, Solan, Himachal Pradesh 173212, India.
E-mail address: pardeepchem@gmail.com (P. Singh).

Peer review under responsibility of King Saud University.

Production and hosting by Elsevier

https://doi.org/10.1016/j.arabjc.2019.08.005

(Gas chromatography–mass spectrometry) elucidation was carried out to expose the possible intermediates formed. Both ZnO/ZF/NG and ZnO/CF/NG were rapidly isolated from the aqueous phase by applying an external magnetic field in 20 sec and 2 min, respectively. The photocatalytic performance and stability of ZnO/ZF/NG and ZnO/CF/NG nanocomposites were confirmed by conducting 10 consecutive regeneration cycles. Owing to recyclability of ZnO/ZF/NG and ZnO/CF/NG, these heterogeneous nanocomposites might be used as cost-effective for treatment of discarded water. The observations endorse that the synthesized ternary heterogeneous nanocomposites facilitates wastewater decontamination using photocatalytic technology.

1. Introduction

Day by day, textiles and printing industries produced a high amount of unconsumed dyes that are settled into the waters. In response, innovation in technology has led to introduction of many toxic waste materials to the environment (Zarrabi et al., 2019; Shandilya et al., 2018a,b; Sudhaik et al., 2018a, b). The immense damage to the aquatic environment was generated by the presence of dyes and pigments in water (Rahman et al., 2016; Prado and Costa, 2009; Raizada et al., 2019; El-Daly et al., 2015). Many factors responsible for coloration of wastewaters are mainly toxicity, chemical oxygen demand (COD), bad smell, high biochemical oxygen demand (BOD), originated from the contaminants (Sudhaik et al., 2018a,b; Gautam et al., 2017; Rahman and Asiri, 2015). Nowadays, for elimination of organic dyes, from different marine environs physicochemical procedures like chemical oxidation, coagulation, membrane separation, photocatalysis, aerobic biological treatments, flocculation, filtration, ozone treatment, chemical oxidation, reverse osmosis, and adsorption have been used. Through these methods, fractional degradation of organic dye and production of a large volume of toxic sludge lead to disposal problem Hasija et al., 2019; Priya et al., 2016; Sharma et al., 2013). Thus for the complete degradation of an organic dye from wastewater, a more capable treatment method is needed (Valtchev et al., 2013; Jamwal et al., 2015; Hasnat et al., 2014).

As a solution to these problems, semiconductor photocatalysis has attracted much attention (Sharma et al., 2019). Underneath ambient conditions and illumination of sunlight, this process is a "green" technology for disintegrating water into hydrogen and oxygen, inactivating viruses and/or entirely excluding all kinds of contaminants (Raizada et al., 2017; Singh et al., 2020; Pare et al., 2009; Yuan et al., 2017; Gu et al., 2013; Rahman et al., 2018). Semiconductor photocatalysis can be fulfilled in the presence of light when band gap of a semiconductor is less than the photonic energy, the valence band electrons are excited to the empty conduction band leading to the creation of electrons-hole pairs. After this, superoxide and hydroxyl radicals are produced by reacting with electrons and holes reacting with oxygen and hydroxyl group, respectively, in water. Thus the reactive oxygen species $OH^{\cdot}$, $^{\cdot}O_2^-$ helps the degrading of organic dye contaminants existing in water (Gupta et al., 2014; Raizada et al., 2017; Nasr et al., 2016; Singh et al., 2017a,b; Shandilya et al., 2018a,b; Rahman et al., 2017a,b; Yamamoto et al., 2013).

Spinel Ferrites have drawn huge attention because of its electrochemical performance, catalytic, excellent chemical stability, narrow band gap and easy availability. Among spinel ferrites, ZF and CF are two mostly utilized magnetic photocatalysts because of their low production expenses, good chemical stability, high coercivity and high Curie temperature (Akhter et al., 2017; Hegazy et al., 2019; P. Singh et al., 2017; R. Singh et al., 2017). For CF, the band gap and positioning of conduction band (CB) and valence band (VB) with respect to redox potential scale are 1.67 eV, 0.14 V and 1.90 V, respectively and 1.90 eV, −1.54 V and 0.38 V for ZF. Therefore, the researchers used the same as photocatalyst because of unreliable benefits of CF and ZF. It is like a challenge to get high photocatalytic performance by exploiting ferrite material alone, due to room temperature ferromagnetism makes magnetically gather these photocatalysts again and fast combination of photogenerated electron-hole pairs (Gautam et al., 2016; Wang et al., 2014; Hussain et al., 2017; Zhu et al., 2016; Jiang et al., 2014). An effective photocatalyst is not proven by the use of ferrite material alone. Thus, even when copper ferrite and zinc ferrite are used alone, photocatalytic degradation is less dominant than the adsorption process (Hong et al., 2016; Raizada et al., 2016; Singh et al., 2020; Chen et al., 2018). Numerous heterojunctions of CF have been reported such as CF/graphene (Gan et al., 2015), TiO_2/CF (Li et al., 2012), and CF/CuS (Kamranifar et al., 2019) to improve its photodegradation activity. In current years, to construct ZF composites, many efforts have been employed for remarkable magnetic and optical properties, such as g-C_3N_4/ZF (Chen et al., 2016), ZnO/ZF (Guo et al., 2014) ZF/TiO_2 (Zhang et al., 2012). A promising approach to boost photocatalytic activity for degrading organic pollutant has been clearly described by these results which point out the introduction of ZF photocatalyst (Dutta et al., 2019; Nada et al., 2017; Singh et al., 2017a,b; Guo et al., 2016).

Meanwhile survey on photocatalytic activity of ZnO explored that it is being used in research laboratory and manufacturing. Thus, Zinc oxide used as a mineral semiconductor because of its 3.30 eV direct band gap along with 60 meV of large exciting binding energy at room temperature. Under the ultraviolet irradiation, ZnO can be used as a photocatalyst effectively, because of its wide band gap. In spite of these outstanding advantages, large direct band gap (3.30 eV) of ZnO reports controlled response for major segment of the solar spectrum, while low degree of electron-hole pair separation, acidic/basic medium prompted corrosion and deactivation during the photocatalytic reactions hampers their extended utility (Rahman et al., 2017a,b; Kavitha and Kumar, 2019). Forming a ZnO heterojunction such as WO_3/ZnO (Liu et al., 2014), TiO_2/ZnO (Qin et al., 2019), BiOCl/ZnO (Chang

et al., 2019) has been displayed the photocatalytic activity and stability of ZnO.

Improved photocatalytic activity and photocatalyst stability, graphene and its conformity are widely used for wastewater treatment. Graphene is a two-dimensional carbon nanofiller with one atom thick planner sheet of sp^2 carbon atoms that are densely packed in hexagonal honeycomb crystal lattice. Graphene has high chemical stability, large theoretical surface area (2630 $m^2 g^{-1}$), mechanical flexibility (1060 GPa), and spacious delocalized π-bonds which increase its conductivity (3000 $W m^{-1} K^{-1}$) and stability (Nasr et al., 2018; Shandilya et al., 2019; Xue et al., 2015). For enhancement in better performance of graphene, doping with a heteroatom, such as N or S increase the pseudo capacitance by deploying its chemical reactivity and electronic properties. NG possess strong chemical stability, rapid electron/ion transport network, large specific surface area and short ion diffusion length. Thus under visible light irradiation NG demonstrate superior photocatalytic activity and excellent adsorption capacity toward organic dyes (Jiang et al., 2017).

On the basis of above discussion it was observed that no one can deduce the recombination of ternary ZnO/ZF/NG and ZnO/CF/NG photocatalyst for better photocatalytic and magnetic recovery performance. The novelty of this work focuses on the evaluation of superior photocatalytic activity of ZnO/ZF/NG and ZnO/CF/NG ternary composite due to following reasons: (i) Band gap of ZF and CF (the band gaps of ZF (Eg = 1.90 eV) and CF (Eg = 1.67 eV) are at lower scale of eV vs Normal hydrogen electrode scale), not suitable for the production of hydroxyl radical and show low absorbance in visible region. Therefore for better photocatalytic activity, we have coupled ZF/CF with ZnO and NG to form ZnO/ZF/NG and ZnO/CF/NG ternary heterostructures, (ii) Magnetic behaviour of ZF and CF: owing to magnetic behaviour of ZF and CF, agglomeration rate of as-prepared ternary nano heterostructure was high. Therefore, ternary nanocomposites ZnO/ZF/NG and ZnO/CF/NG has strong magnetic property which can be easily utilized for separation of charge carriers in photodegradation system (iii) Role of NG: NG provides more surface area to facilitate the better enhancement in photocatalytic activity of loaded magnetic nanoparticle (ZF/CF) and ZnO.

Thus, in this work we have coupled ZnO/CF and ZnO/ZF with NG to improve their photodegradation ability. Malachite dye and Methylene orange dye were opted as target organic dyes to explore the photocatalytic performance of newly synthesized photocatalysts. The degradation kinetics, mechanistic view and recycling efficiency of ZnO/ZF/NG and ZnO/CF/NG were assessed. The influence of adsorption on photodegradation process was also explored.

2. Experimental

2.1. Chemicals and reagents

Cobalt iron (III) oxide (CAS No. 12052-28-7, Purity 99%), Absolute ethanol (CAS No. 64-17-5, Purity 99.5%), Zinc nitrate (CAS No. 10196-18-6, Purity 98%), Potassium hydroxide (CAS No.1310-58-3, Purity 85%), Iron (III) chloride hexahydrate (CAS No. 10025-77-1, Purity 97%), Zinc chloride (CAS No. 7646-85-7, Purity 99.99%), Polyethylene glycol (PEG) (CAS No. 25322-68-3), Iron nitrate (CAS No. 7782-61-8, Purity 99%), Sodium hydroxide (CAS No. 1310-73-2, Purity 50% in H_2O), Citric Acid (CAS No. 77-92-9), Urea (CAS No. 57-13-6), Methylene Orange (MO) (CAS No. 547-58-0, Purity 85%) and Malachite green (MG) (CAS No. 569-64-2) were purchased from Sigma Aldrich, and used devoid of any auxiliary purification.

2.2. Fabrication of ZnO nanoparticles

ZnO nanoparticles were prepared by direct precipitation method. Briefly, an aqueous solution of 0.2 M of zinc nitrate and 0.4 M of KOH were prepared with deionized water respectively. At room temperature, the KOH solution was gradually purred into zinc nitrate solution with constant stirring to form a white suspension. After centrifuging the obtained mixture at 5000 rpm for 20 min and it was washed three times with deionized water and at last with absolute alcohol. Furthermore, the acquired precipitates were calcined at 500 °C for 3 h on a custom made tubular muffle furnace to facilitate formation of ZnO.

2.3. Synthesis of ZF nanoparticles

ZF nanoparticles were prepared in our laboratory by dissolving 4.90 g zinc nitrate and 13.4 g iron nitrate in 50 mL of distilled water. The above solution was poured into aqueous solution of 4.2 g of NaOH in 70 mL distilled water and 3 mL ethylene diamine. Subsequently for achieving complete chelation, this mixed solution was heated at 90 °C for 1 h. Finally, the formed powder was put into an alumina crucible and calcined at 600 °C with heating rate of 10 °C/min for 1 h.

2.4. Synthesis of CF nanoparticles

CF nanoparticles were synthesized by auto combustion method. In brief 1.4 g of cobalt nitrate and 4.04 g of iron nitrate were dissolved in 100 mL deionized water with stoichiometric ratios of 1:2 ([Co]:[Fe]). Then, 0.032 g/mL of citric acid solution was added to the above aqueous mixture under constant magnetic stirring. The molar ratio of cobalt nitrate to citric acid was set to 1:1 for attaining complete combustion process. The mixed aqueous solution was adjusted to pH = 7 using ammonia. After that, the above solution was heated to be converted into a xerogel. After the heating process of died gel, a fluffy powder was formed. Finally as-burnt precursor powder was put into alumina crucible and calcined at 400 °C for 2 h.

2.5. Synthesis of NG nanoparticles

Graphite oxide (GO) was prepared by using modified Hummer's process. NG was fabricated by using GO as raw material and urea as reducing dopant agent in hydrothermal process. In brief, 30 mL of GO and urea with a mass ratio of 1:30 were mixed in a beaker. This above solution was constantly stirred for 30 min. The resulting aqueous solution was transferred into a Teflon lined stainless steel autoclave, sealed and maintained at 160 °C for 3 h. Then, the temperature of autoclave was naturally low to room temperature and the as-synthesized NG

was taking out with a tweezer. Afterwards, as-synthesized NG nanoparticles were dipped into distilled water and washed fully to remove any unreacted urea. For removing surface adsorbed water, NG nanoparticles were blotted with filter paper and freeze-dried under vacuum to get the final products. The final product was named as NG nanoparticles.

2.6. Synthesis of ZnO/ZF/NG and ZnO/CF/NG nanocomposites

Firstly, 0.5 g of CF/ZF and 8.37 g of $ZnCl_2$ were dispersed in 50 mL of PEG (polyethylene glycol, MW-400 g mol^{-1}) followed by 20 min ultrasonication. Well dispersed nanoparticles of CF/ZF and $ZnCl_2$ in PEG solution were obtained due to ultrasonication. The obtained solution was poured into Teflon lined container that had been pre-heated at 150 °C kept in an oven. In another beaker, 0.5 g of NG was dispersed in 20 mL absolute ethanol and then sonicated for 45 min. After this, the above two solutions were mixed followed by dropwise addition of NH_4OH with continuous stirring of 6 h. The solution pH was maintained 10.0 utilizing NaOH solution (6 M) followed by addition of 1 g of urea. After this, centrifugation of Reaction mixture was done for 15 min at 14,000 rpm at ambient temperature. The supernatant liquid was decanted off from resultant precipitates. The resultant precipitates were repeatedly washed with deionized water and at last with ethanol. The calcination of the resultant precipitates was performed on alumina crucible at 500 °C for 2 h in a custom made tubular muffle furnace to ease the development of one dimensional ZnO/CF/NG or ZnO/ZF/NG nanostructure. The resultant product was named as ZnO/CF/NG or ZnO/ZF/NG.

2.7. Characterization

The crystalline nature of the products was assessed at room temperature by XRD model Siemens D-5000 diffractometer with Cu Kα radiation (l = 1.5406 Å). Surface morphology was observed by scanning electron microscopy (SEM, Model Nava Nano SEM-45 (USA) system). HRTEM imaging analysis was conducted using Tecnai G2 F20 high resolution transmission electron microscope operated at 200 kV accelerating voltage under vacuum conditions. The functional groups were investigated by Fourier transform infrared (FTIR) spectroscopy (Perkin-Elmer Spectrophotometer Spectrum One) was performed the range of 4000–450 cm. The X-ray photoelectron spectra; (XPS) studies were executed with a photoelectron spectrometer (Thermol scientific Escalab 250Xi) exploiting Al Kα radiation for analyzing the surface components and their valence distributions. The UV–vis diffused reflectance spectra were obtained on UV–vis spectrophotometer (Shimadzu, UV-3600). The magnetic properties of synthesized nanocomposites were measured by a magnetic measurement instrument (MPMS-XL-7, Quantum Design).

2.8. HPLC and LCMS analysis

The degradation fragments during mineralization process were analyzed by high performance liquid chromatography (Water HPLC, Austria) equipped with manual injector and photodiode array detector model. The apparatus was packed with Rheodyne manual injector kit and C18 column (5 μm, 25 cm length and 7 mm diameter). The LC-MS analyses were carried out on JEOL GCMATE II GC–MS with a high resolution data system, double focusing instrument with electrospray ionization (ESI) and C18 column (150 mm × 2 mm) (injection volume 20 μL).

2.9. Evaluation of photocatalytic activity

MO and MG dyes were opted as the target pollutants to examine the photodegradation efficiency of as-synthesized ZnO/ZF/NG and ZnO/CF/NG. The experiments were executed in a modest photocatalytic reactor exploiting a 10 W LED lamp (400 nm < wavelength < 700 nm) as the source of visible light. All degradation experiments were performed under atmospheric conditions with a constant stirring speed of 250 rpm. In the case of MO degradation experiments, 50 mg of photocatalyst was purred into 150 mL of an aqueous MO solution (10 mg/L). The above solution was magnetically agitated in darkness for 30 min to attain adsorption and desorption equilibrium. After this, the dispersion solution was sonicated for 10 min. Then the catalyst containing MO solution was placed under UV irradiation with stirring facility. Throughout the degradation process, 5 mL of solution was removed from mixture and centrifuged it for 15 min in 3500 rpm. Lastly, the supernatant liquid was obtained and the concentration of the dye was determined by UV–vis spectrophotometer. The photocatalytic performance of catalyst was calculated by using following equation (Singh et al., 2013).

$$\text{Degradtion Efficiency } (\%) = \frac{\text{Co} - \text{C}}{\text{Co}} \times 100 \quad (1)$$

where C_0 and C is the concentration of initial and degraded dye in solution, respectively. Similarly, the photodegradation of MG was also monitored by following the above procedure.

3. Results and discussion

3.1. Characterization of ZnO/ZF/NG and ZnO/CF/NG nanocomposites

3.1.1. Xrd

X-ray diffraction analysis was conducted for the determination of crystal structure and phase purity of the produced samples. The XRD pattern of pure CF, pure ZF, NG, ZnO/ZF/NG and ZnO/CF/NG nanostructures were illustrated in Fig. 1. The crystal plane of pure CF (JCPDS No. 22-1086) with diffraction peaks at 2θ = 30.1°, 35.6°, 43.2°, 57.0° and 62.7° represented (2 2 0), (3 1 1), (4 0 0), (5 1 1) and (4 4 0), respectively (Borgohain et al., 2012). For the planes of pure ZF (JCPDS No. 22-1012), noticeably, all diffraction peak at 2θ = 35.3° and 62.2° were observed which respectively matched exactly with the crystallographic planes of (3 1 1) and (4 4 0); (Huang et al., 2015). The pure nitrogen-doped graphene showed intense peak at 2θ = 26.3° which corresponds to the (0 0 2) crystallographic planes. This diffraction peak confirms that nitrogen atoms have come into the crystal lattice of graphite which produced the increased distance between the graphite layers (Yao et al., 2017). In case of ZnO/ZF/NG nanocomposites, all diffraction peaks correspond to hexagonal phase of zinc oxide (peaks at 2θ = 31.8° and 62.8° can be indexed to the planes of (1 0 0) and (1 0 3) respectively), nitrogen-doped graphene (NG) (peak at 2θ = 26.3° of plane

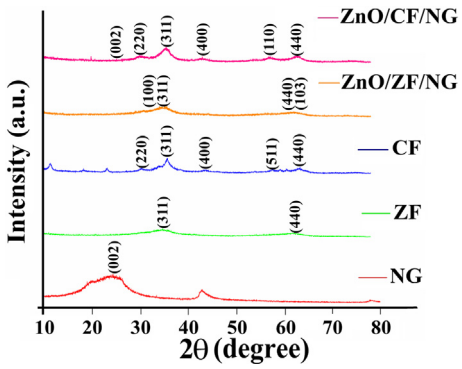

Fig. 1 XRD patterns of NG, ZF, CF, ZnO/ZF/NG and ZnO/CF/NG nanocomposites.

(0 0 2)) and crystal plane of pure ZF (JCPDS No. 22-1012) (peaks at 2θ = 35.3° and 62.2° represented (3 1 1) and (4 4 0) planes) (Sathishkumar et al., 2013). The XRD diffraction pattern of ZnO/CF/NG nanocatalysts showed peaks almost matching with respect to structure of ZnO (peak at 2θ = 56.6° corresponds to (1 1 0) plane), matches with CF (peaks at 2θ = 30.1°, 35.6°, 43.2° and 62.7° corresponds to (2 2 0), (3 1 1), (4 0 0) and (4 4 0) planes) and matches with only one peak of NG nanoparticles (peak at 2θ = 26.3° corresponds to (0 0 2) plane) (Singh et al., 2017a,b). Particle size of nanocomposites were also calculated by Scherrer equation:

$$t = \frac{k\lambda}{dCos\theta} \tag{2}$$

here t is a measure for the dimension of the particle in the direction perpendicular to the reflecting plane, K is a constant (often taken as 1 or 0.9), λ is the X-ray wavelength, d is the peak width and θ is the angle between beam and normal on the reflecting plane. The average crystallite size of nanocomposites ZnO/CF/NG was 0.042 nm and for ZnO/ZF/NG was 0.84 nm calculated by Scherrer equation

3.1.2. TEM and SEM analysis

TEM analysis of NG, ZnO/CF/NG and ZnO/ZF/NG was depicted in Fig. 2(a–f). The curled sheet like structure of NG could be seen in Fig. 2(a). The TEM image of ZnO/CF/NG nanoparticles also revealed that CF nanoparticles (black patches) and ZnO particles (gray patch) have gathered on the surface of NG to form a core–shell like structure. As seen in Fig. 2 the dispersion of both ZF and ZnO was observed onto NG sheet. The d-spacing values were calculated from lattice plane fringes. The measured d-spacing of 0.296 nm resembled to the lattice spacing of (2 2 0) plane of CF. The fringe with d-spacing of 0.476 nm was corresponded to lattice spacing (1 1 1) of cubic nanostructured ZF whilst the lattice fringe of 0.268 nm assigned to the (0 0 2) plane of ZnO (Wang et al., 2017). Thus nanocomposites have a spherical morphology and average size particles.

The morphology of NG, ZnO/CF/NG and ZnO/ZF/NG was investigated by SEM. As shown in Fig. 3(a–b), NG nanosheet, were loosely loaded like fragments of foam. The loading of CF, ZF, and NG was clearly seen in ZnO/CF/NG and ZnO/ZF/NG. A core-shell structure was seen on the surface of NG by the deposition of CF in ZnO (Sathishkumar et al., 2013). It was also seen that some ZF nanosphere particles collapsed within NG stop the accumulating of particles. It was noted that some ZF nano spheres were compressed within NG and prevent of particles. It was also observed that CF or ZF, ZnO nanoparticles were dispersed on NG surface from Fig. 3(a–b). Also, FESEM image of NG, ZnO/CF/NG and ZnO/ZF/NG observed different shaped agglomerated in Fig. 3(b, d, and f).

3.1.3. FT-IR spectra

Fig. S1 displayed FT-IR spectra of ZnO/CF/NG, ZnO/ZF/NG, CF, ZF, and NG. FTIR spectrum of pristine NG depicted typical stretching bands of C═C at 1400 cm^{-1}. The other peaks at 1180 cm^{-1} and 1565 cm^{-1} corresponded to C—N and C═C bond (Singh et al., 2017a,b). FTIR spectrum of CF revealed peaks in the range of 572–435 cm^{-1} which corresponded to Fe—O bonds (Kachi et al., 2019). Two characteristic peaks at 579 cm^{-1} and 1480 cm^{-1} which assigned to metal-oxygen vibration and —OH bending, respectively in CF. The peak observed below at 580 cm^{-1} ascribed to Zn—O stretching vibration (Zamiri et al., 2017). ZF had two peaks at 600–500 cm^{-1} and 3450 cm^{-1} which point out the metal-oxygen vibration and O—H stretching vibration, respectively. In the spectrum of CF/ZnO nanostructure, a wide peak was seen at 3400 cm^{-1} due to the strong O—H stretching band (Borgohain et al., 2012).

3.1.4. UV–visible analysis

The optical transmittance absorption properties of the as-prepared CF, ZF and ZnO are examined at room temperature by UV–vis spectroscopy. As shown in Fig. S2a absorption spectrum can be observed in UV–visible range from 200 to 800 nm for ZF, CF, and ZnO. In addition, using the absorption data, the band gap energy can be computed exploiting the Tauc's equation, given below

$$\alpha hv = A\left(hv - E_g\right)^{\frac{n}{2}} \tag{2}$$

where a is absorption coefficient, hv is photon energy, E_g indicates optical band gap of material and A signifies a constant comparative to the material. For ZnO, absorption peak at 375 nm was ascribed to band gap of 3.14 eV (Ferdosi et al., 2019). CF and ZF have broadband spectra in 200–800 nm and ZnO/CF and ZnO/ZF have aobsortion in UV and visible region (Fig. S2b). ZF had maximum absorption at 371 nm and calculated optical band gap of ZF was 1.88 eV (Wang et al., 2017) (Fig. S2c). The band gap of CF was 1.70 eV calculated by Tauc's plot (Ferdosi et al., 2019) (Fig. S2d). These results of UV–vis spectroscopy confirmed the presence of CF, ZF, and ZnO in the heterojunction nanocomposites. The photoluminescence spectra of ZF and CF displayed high intense peak which revealed that bare ZF and CF exhibited high. Electron-hole pair separation and photodegradation efficiency of semiconductor was analyzed by PL spectrum. Fig. S3 explored the PL spectra of CF, ZF, ZnO, ZnO/CF/NG and ZnO/ZF/NG photocatalysts. It was observed from the spectra that luminescence peak intensity of ZnO/CF/NG and ZnO/ZF/NG was lower than CF, ZF, ZnO photocatalysts. Luminescence spectra of semiconductor typically deals with photogenerated electron-hole pair separation, thus from the results it was confirmed that ZnO/CF/NG displayed improved degradation efficiency

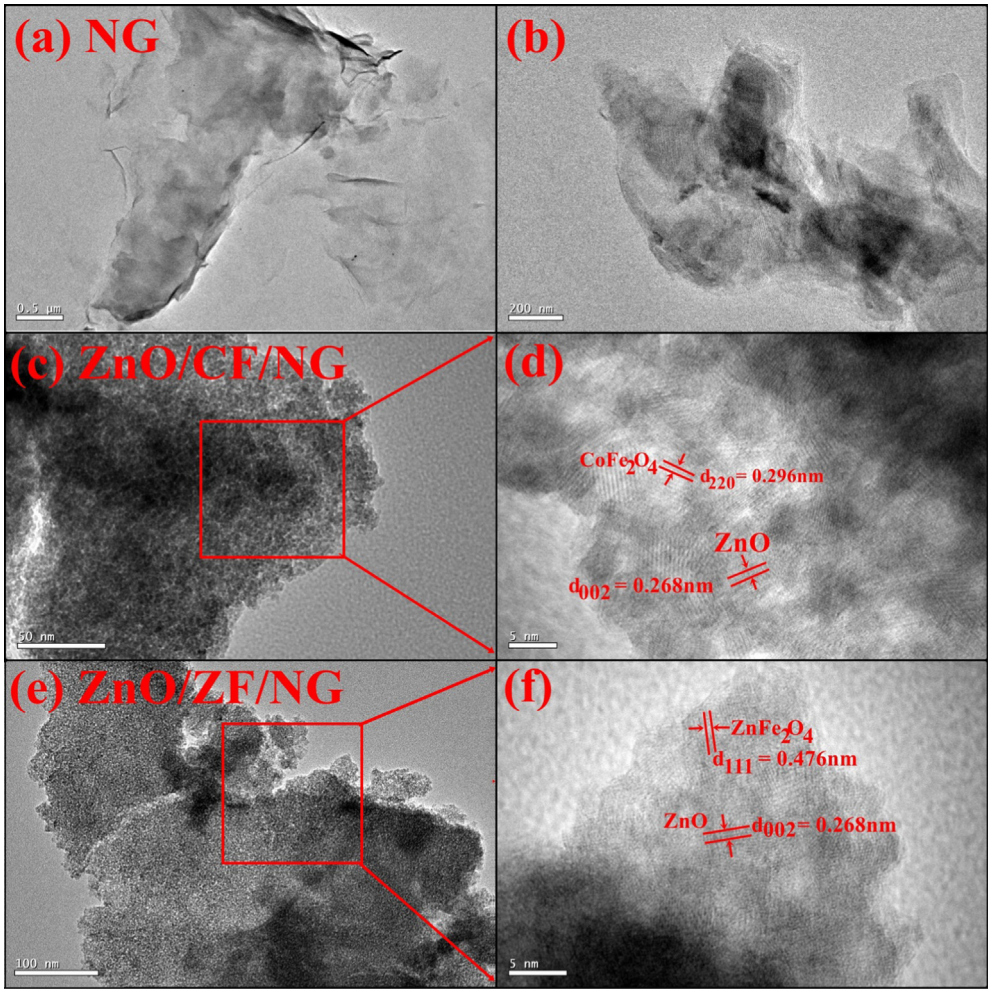

Fig. 2 TEM images of (a) NG, (b) High resolution image of NG, (c) ZnO/CF/NG, (d) High resolution image of selected area (c), (e) ZnO/ZF/NG and (f) High resolution image of selected area (e).

than ZnO/ZF/NG, as well as both the nanocomposites exhibited better photodegradation efficacy than bare photocatalysts.

3.1.5. XPS analysis

XPS analysis was conducted to explore the chemical components and oxidation states of carbon, oxygen, cobalt, iron, zinc, silver and nitrogen elements. Fig. 4(a–f) exhibits the whole spectra of ZnO/CF/NG and ZnO/ZF/NG nanocomposites. In the case of C1 s, the peaks positioned at 282 eV was assigned to sp^2 (sp^2C) carbons atom bonded to nitrogen in NG (Mou et al., 2011) (Fig. 4a). In Fig. 4b spectra of O 1s, the peak centred at 527 eV corresponds to lattice oxygen of ZnO, CF and ZF (Wang et al., 2017). In Fig. 4c the peaks at 778 eV and 793 eV were respectively assigned to Co $2p_{3/2}$ and Co $2p_{1/2}$. These two peaks were representative peaks of Co $2p^3$. As showed in Fig. 4d the peaks appeared at 708 eV and 722 eV respectively belonged to Fe $2p_{3/2}$ and Fe $2p_{1/2}$. Introduction of CF in complex was confirmed by the peaks of Co $2p^3$ and Fe $2p^3$ (Jing et al., 2016). In Zn $2p^3$ spectra, the peak at 1019 eV and 1042 eV were respectively assigned to binding energy of Zn $2p_{3/2}$ and Zn $2p_{1/2}$ (Wang et al., 2017) (Fig. 4e). Moreover, an N 1s, the peak at 397 eV was corresponding to the formation of N—C bonds in NG (Guo et al., 2013) (Fig. 4f).

3.2. Photocatalytic and adsorption removal of MG and MO

The results of the photocatalytic activity of prepared photocatalysts were assessed by the photodegradation and adsorption of malachite green and methyl orange dyes under different conditions as shown in Fig. 5(a–f). Fig. 5(e and f) presents the results of MO and MG photodegradation under 100 W halogen lamp. Both ZnO/ZF/NG and ZnO/CF/NG show significant activity for MO and MG dye photodegradation. For MG photodegradation, following trend was obtained in the reaction time period of 140 min: ZnO/CF/NG (98%) > ZnO/ZF/NG (92%) > CF (50%) > ZnO (49%) > ZF (48%) > NG (30%). In case of MO degradation, removal efficiency had following order for 140 min of photocatalysis: ZnO/CF/NG (99%) > ZnO/ZF/NG (94%) > CF (52%) > ZnO (50%) > ZF (49%) > NG (30%). Ternary photocatalyst ZnO/CF/NG and ZnO/ZF/NG had dominated the photocatalysis. While no degradation in absence of photocatalysts confirmed the stability of MG and MO under visible light

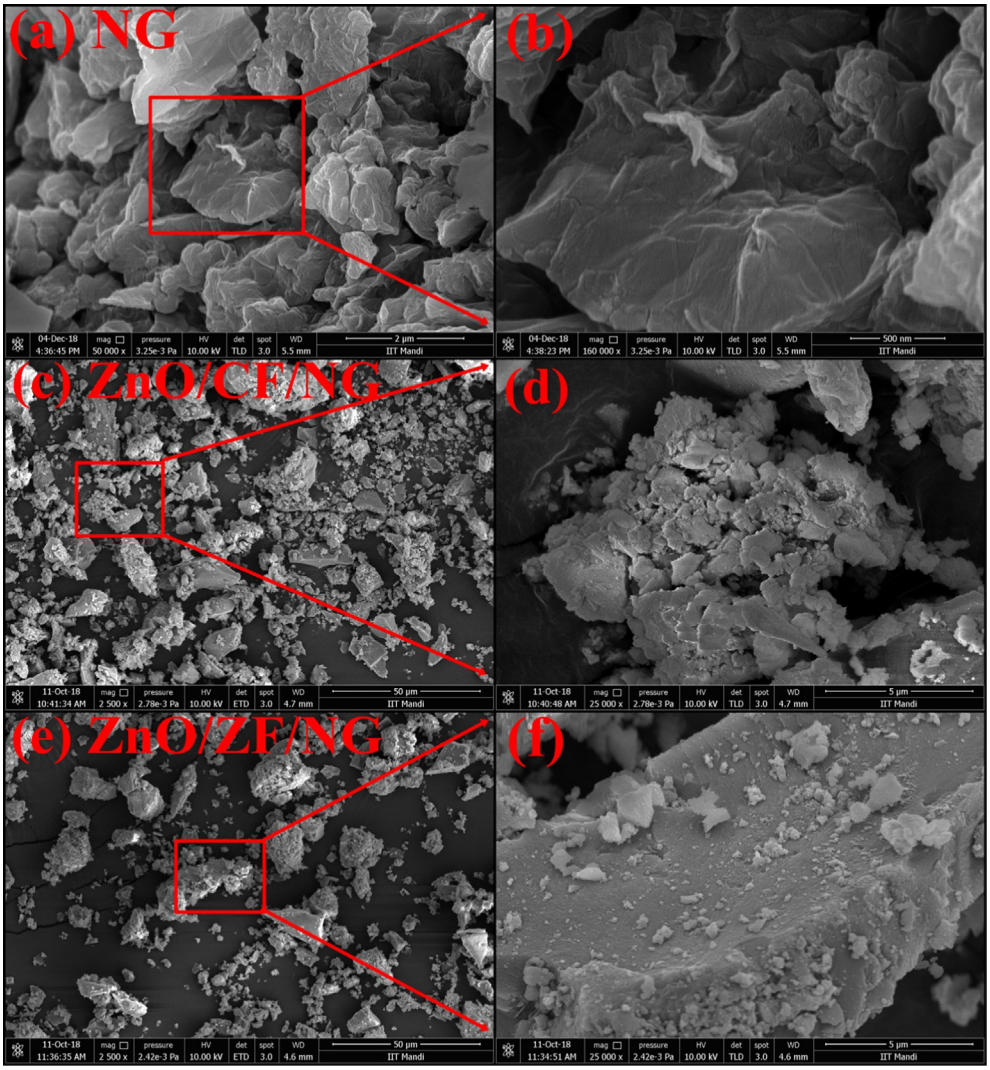

Fig. 3 SEM and FESEM images of (a) NG, (b) High resolution image of selected area (a), (c) ZnO/CF/NG, (d) High resolution image of selected area (c), (e) ZnO/ZF/NG and (f) High resolution image of selected area (e).

(Fig. 5a and b) Moreover, adsorption experiments were also executed to see the effect of adsorption of MG and MO removal. From adsorption experiment, it was concluded that ZnO/ZF/NG, ZnO/CF/NG and NG had significant adsorption ability for MG and MO removal while ZnO, CF, and ZF had removal efficiency below 10%. The integration of NG with ZnO/ZF and ZnO/CF had resulted in significant improvement in adsorption ability of photocatalysts (Fig. 5c and d). The pseudo first order and second order kinetics for adsorption rate (Lu et al., 2014; Singh et al., 2019a) is described by Eqs. (3) and (4):

$$(q_e - q_t) = \log q_e - \frac{k_1 t}{2.303} \tag{4}$$

$$\frac{t}{q_t} = \frac{1}{k_1 q_e^2} + \frac{t}{q_e} \tag{5}$$

where q_e (mg/g) denotes the amount of MG/MO adsorbed per gram of adsorbent at equilibrium, q_t (mg/g) is the amount of dye adsorbed at time, t, and k_2 (g/mg min) indicates second order constant. The kinetic parameter adsorptions of MG/MO are summarized in Table 1. The adsorption of MG and MO onto surface obeyed the pseudo-second-order kinetics. The adsorption process may proceeds through chemical sorption, involving valence forces via sharing or exchanging of electrons between dye molecules and adsorbent. ZnO/CF/NG, ZnO/ZF/NG, and NG had an adsorptive capacity of 65.12, 66.00, and 67.00 mg/g for MB, respectively. 62.30, 58.29 and 66.00 mg/g of MO were adsorbed onto ZnO/CF/NG, ZnO/ZF/NG and NG, respectively.

Initial reaction pH plays a crucial role in both adsorption and photocatalysis of dyes onto adsorbent surface (Table 2). In present work, pH was varied from 2 to 9. The adsorption of MG was maximum at pH 7, while during MO adsorption, the removal rate was higher at pH 4. Moreover, zeta potential analysis was used to find the pH of zero point charge. The pH_{zpc} values of ZnO/CF/NG, ZnO/ZF/NG and NG was found to be 6.7, 6.7, and 6.7. Above pH_{zpc}, the adsorbent surface was negatively charged and facilitated the adsorption of cationic MG dye. On the other side, below pH_{zpc}, positively charged surface of adsorbent facilitated the adsorption of anion MO dye.

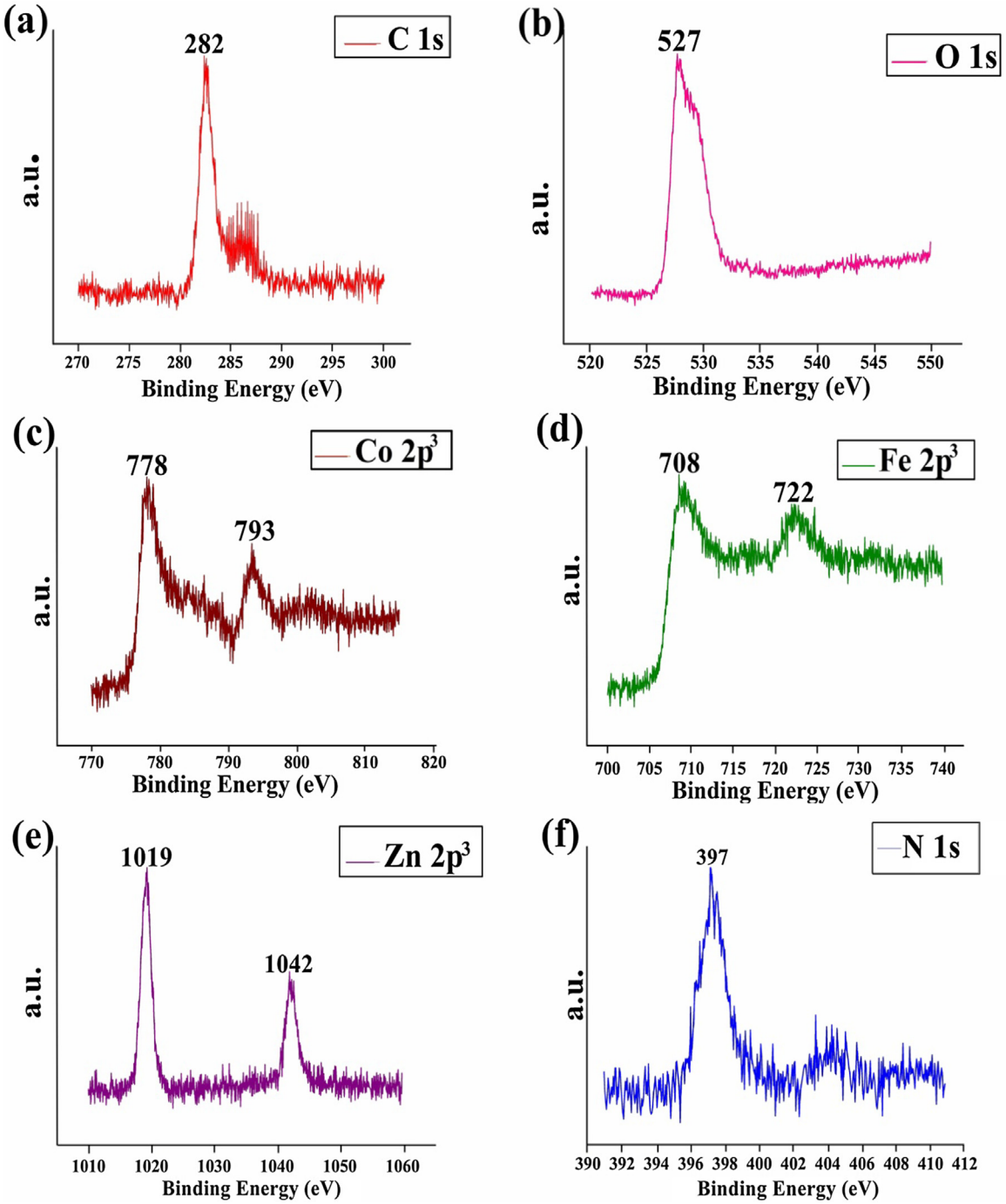

Fig. 4 XPS spectra of ZnO/ZF/NG and ZnO/CF/NG showing presence of (a) C 1s, (b) O 1s, (c) Co $2p^3$, (d) Fe $2p^3$, (e) Zn $2p^3$ and (f) N 1s elements.

3.3. Synergy between adsorption and photocatalysis and mineralization of dyes

It is well documented that photocatalytic activity of the photocatalysts is greatly impressed by the adsorption of organic contaminants onto photocatalysts surface (Shandilya et al., 2018a, b). Therefore, the photodegradation of MG and MB was subjected to two different reaction criteria: (i) adsorption followed by photocatalysis and (ii) concurrent adsorption with photocatalysis (A + P) process. From Fig. 5, it is obvious that A + P processes are more efficient for photocatalytic degradation of MO and MG dye. During A-P process, the excessive adsorption of dye molecules onto photocatalysts surface acted as screen for visible light and overall photoactivity was reduced; while in case of A + P, adsorbed dye molecules were concurrently photodegraded by photocatalysts under halogen lamp. Thus, it was concluded that ZnO/ZF/NG/A + P and ZnO/CF/NG/A + P were efficient for photocatalytic degradation of MG and MO degradation. Further studies were carried out with ZnO/ZF/NG and ZnO/CF/NG photocatalysts under

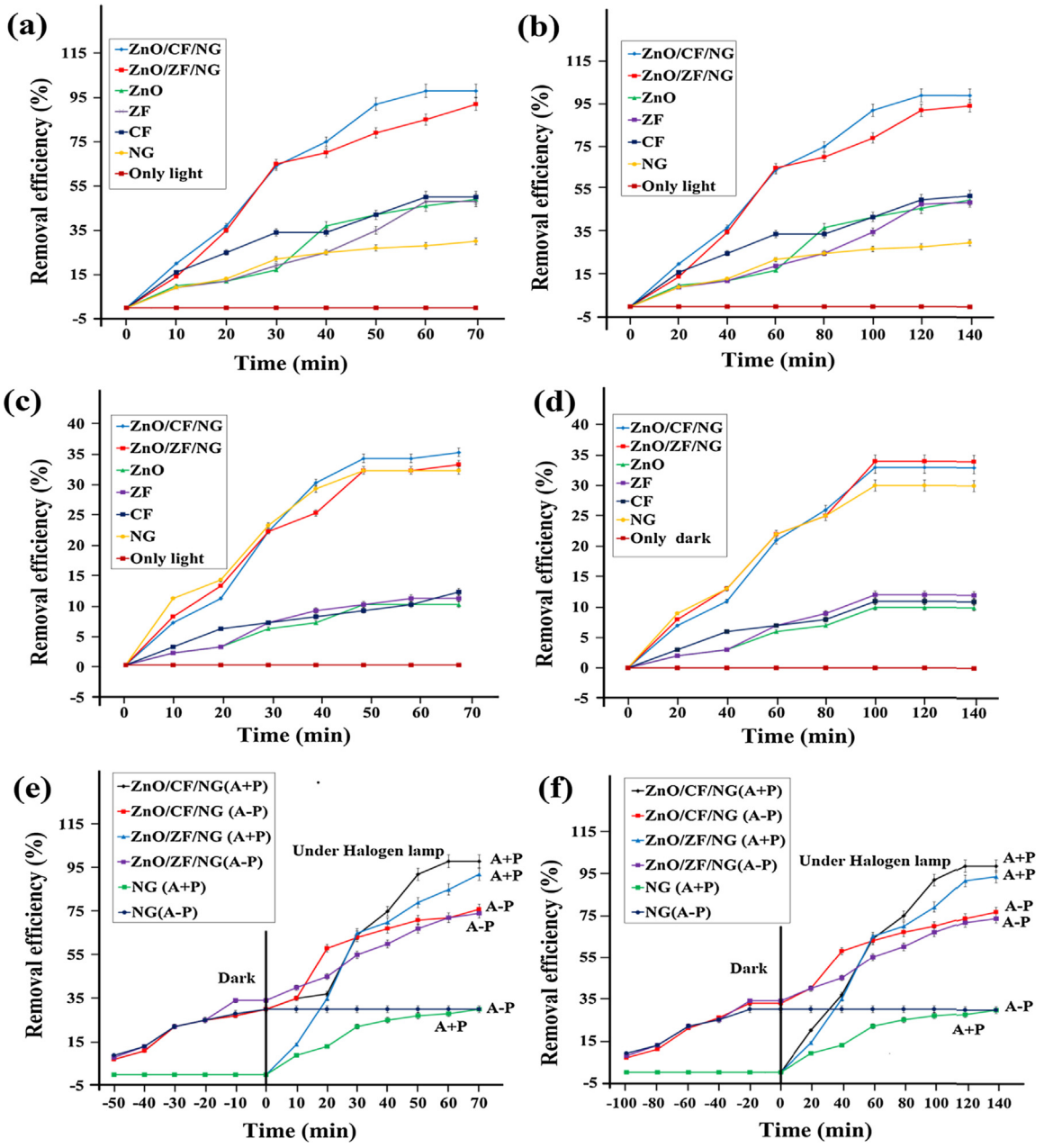

Fig. 5 Removal of MG and MO under different reaction conditions: Photocatalytic degradation of MG (a), MO (b), removal of MO (c) and MG (d) using adsorption process, Effect of adsorption on photocatalytic removal of MG (e) and MO (f). Reaction conditions: [MO] = 1.5×10^{-5} mol dm^{-3}; [MG] = 1×10^{-5} mol dm^{-3}; [catalyst] = 50 mg/100 mL; pH = 4.0(MO); 6 (MG); reaction time = 70 min (MG) and 140 min (MO), Light Intensity = 750 lx.

simultaneous and adsorption. The degradation kinetics MG and MO was investigated using Eq. (6) (Raizada et al., 2014a,b).

$$-\ln\left(\frac{C}{C_0}\right) = kt \tag{6}$$

The linearity of $-\ln(C/C_0)$ *versus* time (t) plot describes pseudo first order kinetics controls degradation process. The rate constants, 0.034 and 0.032 min^{-1} was obtained for MG degradation using ZnO/ZF/NG (R^2, 0.96) and ZnO/CF/NG (R^2, 0.98) photocatalyst, respectively (Table 3); while ZnO/ZF/NG (R^2, 0.97) and ZnO/CF/NG (R^2, 0.98) had rate constants, of 0.26 and 0.29 min^{-1}, respectively, for MO photodegradation (see Table 4). The dye degradation involves both decolorization and breaking of aromatic compounds into simpler inorganic moieties. To confirm the breaking of aromatic compounds, COD removal experiments were performed. 99% and 98% of COD was removed during MG mineralization process using ZnO/ZF/NG and ZnO/CF/NG respectively, in 140 min; while in the case of MO mineralization, ZnO/ZF/NG and ZnO/CF/NG had 99% and 98% of respective COD removal in 300 min (Fig. 6a and b).

Table 1 Kinetics for MG and MO on various adsorbents. Reaction condition: [MO] = 1.5×10^{-5} mol dm^{-3}; [MB] = 1×10^{-5} mol dm^{-3}; [catalyst] = 50 mg/100 mL; pH = 4.0(MO); 6 (MB); reaction time = 70 min (MG) and 140 min (MO).

	Pseudo first order kinetics					
	$k_1(min^{-1})$		$q_e(mg/g)$		R^2	
	MG	MO	MG	MO	MG	MO
ZnO/CF/NG	0.0179 ± 0.0011	0.0171 ± 0.0010	64.00	65.12	0.91 ± 0.10	0.92 ± 0.11
ZnO/ZF/NG	0.0173 ± 0.0012	0.0174 ± 0.0013	62.56	66.00	0.93 ± 0.12	0.90 ± 0.13
NG	0.0171 ± 0.0014	0.0175 ± 0.0012	63.00	67.10	0.90 ± 0.13	0.91 ± 0.14
	Pseudo second order kinetics					
	$k_2(g/(mg\ min)$		$q_e(mg/g)$		R^2	
	MG	MO	MG	MO	MG	MO
ZnO/CF/NG	0.00025 ± 0.0013	0.00017 ± 0.0011	67.40	64.30	0.99 ± 0.11	0.96 ± 0.12
ZnO/ZF/NG	0.00015 ± 0.0010	0.00011 ± 0.0015	65.00	65.29	0.96 ± 0.14	0.97 ± 0.13
NG	0.00005 ± 0.0011	0.000078 ± 0.0014	66.00	66.00	0.97 ± 0.15	0.98 ± 0.12

Table 2 Effect of pH of MB and MO adsorption onto photocatalysts. Reaction condition: [MO] = 1.5×10^{-5} mol dm^{-3}; [MB] = 1×10^{-5} mol dm^{-3}; [catalyst] = 50 mg/100 mL; pH = 4.0(MO); 6 (MB); reaction time = 70 min (MG) and 140 min (MO).

pH	Removal efficiency of ZnO/CF/NG (%)		Removal efficiency of ZnO/ZF/NG (%)		Removal efficiency of NG (%)	
	MG	MO	MG	MO	MG	MO
4	15	33	12	34	16	31
6	25	25	20	25	22	30
7	34	17	34	18	30	28
8	36	10	37	10	32	25
9	36	10	37	9	32	22

Table 3 Kinetic parameter for photocatalysis of dyes during A + P process. Reaction condition: [MO] = 1.5×10^{-5} mol dm^{-3}; [MB] = 1×10^{-5} mol dm^{-3}; [catalyst] = 50 mg/100 mL; pH = 4.0(MO); 6 (MB); reaction time = 70 min (MG) and 140 min (MO), light intensity = 750 lx.

Dye (Pollutants)	Photo-catalyst	R^2	k (min^{-1})
MG	ZnO/ZF/NG	0.96	0.034
	ZnO/CF/NG	0.98	0.032
MO	ZnO/ZF/NG	0.97	0.026
	ZnO/CF/NG	0.98	0.029

3.4. Detection of reactive species and possible mechanism for photocatalytic degradation

As evidenced from previous work, photocatalytic degradation of dyes was mainly due to presence of reactive oxidative species like electrons (e^-_{CB}), holes (h^+_{VB}), hydroxyl radicals ($OH^\cdot$ and superoxide radicals ($O_2^{\cdot-}$). In present work, Cr(VI) ion, ammonium oxalate(AO), isopropyl alcohol (IPA), and benzoquinone (BZQ) were respectively used as trapping agents for e^-_{CB}, h^+_{VB}, $OH^\cdot$, and $O_2^{\cdot-}$ scavenger (He et al., 2014; Pare et al., 2008). During scavenging experiment for ZnO/ZF/NG, removal efficiency was decreased to 16% (MO dye) and 15% (MG dye) with addition of IPA and BZQ to the reaction solution. While in case of ZnO/CF/NG, 17% and 18% of removal efficiency was found for addition of IPA and BZQ scavengers, respectively (Fig. 6c and d). On the other hand, AO and Cr (VI) had no significant effect on photodegradation of MO and MG dyes under halogen lamp (Fig. 6c and d). The scavenging experiments confirmed the presence of $OH^\cdot$ and $O_2^{\cdot-}$ as main reactive species in MO and MG photodegradation (Fig. 6e and f).

3.5. Possible photocatalytic mechanism of ZnO/ZF/NG and ZnO/CF/NG

3.5.1. Type II scheme approach for ZnO/ZF/NG

The detailed mechanistic route of photocatalytic processes was displayed in Fig. 7a. The oxidation potential of VB and reduction potential of CB in ZF were found to be +0.38 V and −1.54 V, respectively, whilst positions of VB maximum and CB minimum of ZnO were +2.7 and −0.5 V (Kachi et al., 2019; Wang et al., 2017). Because of the strong interfacial contact and positioning of CB on redox scale, photoexcited electrons from ZF were shifted to CB of ZnO. On the other hand, the holes from ZnO were moved towards the VB of ZF photocatalyst. Therefore, electron–hole recombination was avoided by the formation of heterojunction-type II. Graphene has already been reported to have a sink behavior for photogenerated electrons (Shandilya et al., 2019). However in this surface assisted photocatalytic mechanism, graphene acted as a surface supported for ZnO and ZF photocatalyst. Due to the negative reduction potential in CB of ZnO, photogenerated electrons reacted with molecular O_2 to produce $O_2^{\cdot-}$ radicals. The photogenerated holes in VB of ZnO and $O_2^{\cdot-}$ radicals were lead to degradation of organic dye and mineralize it

Table 4 Comparison of mineralization of few colored industrial effluents and standard dyes MO as well as MG with prepared ZnO/ZF/NG and ZnO/CF/NG.

S. no.	Composite	Targeted dye	Source of light	Photodegradation efficiency	Degradation time	References
1.	ZnO/CF	Direct Blue 71	150 W, Tungsten halogen lamp	100%	5 h	Sathishkumar et al., 2013
2.	CF/Graphene	Methylene Blue (MB)	Tungsten halogen lamp	100%	3 h	Gan et al., 2015
3.	CF/ZnO	Acid Violet, Acid Brown	UV–Visible	76% 63%	100 min	Ferdosi et al., 2019
4.	CF/ZnO	Phenolphthalein	UV radiation	89%	1 h	Borgohain et al., 2012
5.	ZF/$FeFe_2O_4$/ZnO	Azo Textile Dye F3B	UV Radiation	90%	140 min	
6.	Ag_3PO_4/ZF	MB, Rhodamine B (Rh B)	LED light	100%	60 min	
7.	ZF/Graphene	Rh B, MB, MO	Visible light	100%	120 min	Lu et al., 2014
8.	Fe_2O_4/ZnO/ZF	Rh B, MO	Visible light	95.2% 52.3%	60 min	
9.	**ZnO/ZF/NG**	**MG, MO**	**Halogen lamp**	**92%** **94%**	**140 min**	
10.	**ZnO/CF/NG**	**MG, MO**	**Halogen lamp**	**98%** **99%**	**140 min**	

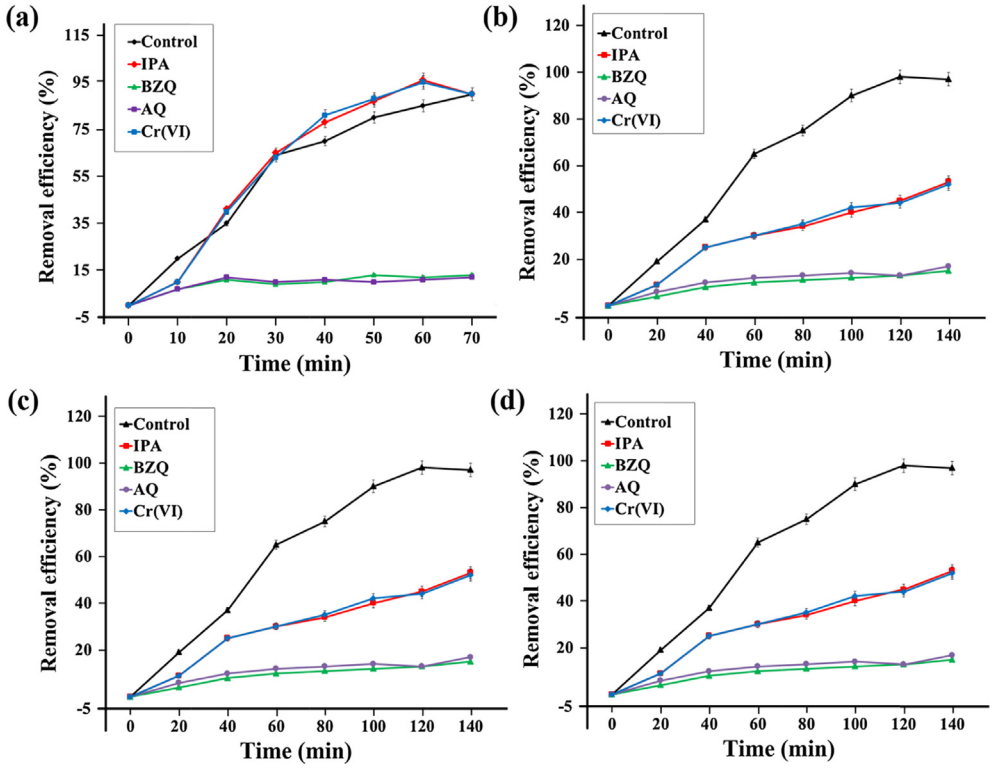

Fig. 6 (a) COD removal during MO mineralization, (b) COD removal during MG mineralization. Scavenging experiment during ZnO/ZF/NG assisted photocatalysis for (c) MG and (d) MO degradation. Scavenging experiment during ZnO/CF/NG assisted photocatalysis for (e) MG and (f) MO degradation. Reaction conditions: [MO] = 1.5×10^{-5} mol dm^{-3}; [MG] = 1×10^{-5} mol dm^{-3}; [catalyst] = 50 mg/100 mL; pH = 4.0(MO); 6 (MG); reaction time = 70 min (MG) and 140 min (MO), [IPA] = 1.0×10^{-5} mol dm^{-3}, [BZQ] = 2.0×10^{-5} mol dm^{-3}, [Cr(VI)] = 1.0×10^{-5} mol dm^{-3}; [AO] = 1.5×10^{-5} mol dm^{-3}, Light Intensity = 750 lx.

into degraded products. The improved photocatalytic performance can be explained by two main reasons as can be concluded from the observations. First, because of the lower band gap of the nanocomposite, higher numbers of photons are absorbed which can raise photocatalytic activity. Second, the interdependent influence of ZnO, NG and ZF semiconduc-

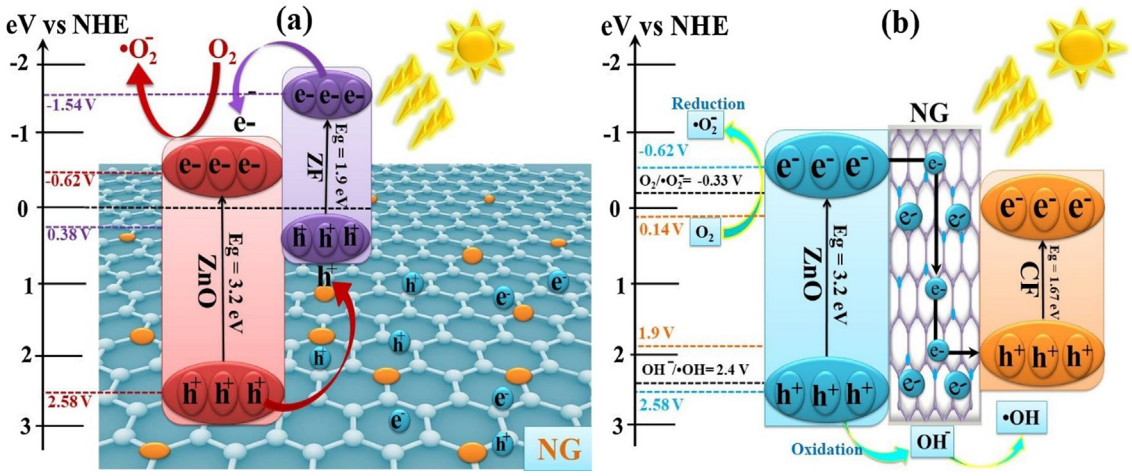

Fig. 7 Mechanistic view of photocatalytic degradation of pollutants using (a) ZnO/ZF/NG and (b) ZnO/CF/NG nanocomposites.

tors could prohibit electron–hole pair recombination by charge transfer process.

3.5.2. Z-scheme approach for ZnO/CF/NG

The two semiconductors which having proper band gap energies assimilating to form heterostructure of Z-scheme type, which improve the separation efficiency of photogenerated charge carriers, and hereby enhance the photocatalytic activity of synthesized system. In Fig. 7b, a proposed schematic shows a possible photocatalytic mechanism of electron and hole formation and their reactions with water and oxygen. The positioning of CB and VB with respect to redox potential scale were 0.14 V and 1.9 V for cobalt ferrite (CF), whilst positions of CB minimum and VB maximum of ZnO were −0.62 V and 2.58 V (Ferdosi et al., 2019; Wang et al., 2017). As the CF has narrower band gap than ZnO and NG can act as ideal electron surface mediator between these two semiconductors due to its superpriorites in photochemical and conductivity properties (Shandilya et al., 2019; Singh et al., 2019b). The band potential of p-type semiconductor CF and n-type semiconductor ZnO ultimately satisfied the requirements of Z-scheme. Under visible light irradiation, transferring photoinduced electrons may happen from the conduction band of ZnO to the valence band of CF. On the other hand, the transferring hole happens from more anodic valence band of ZnO to the valence band of CF. Therefore, the recombination of electron-hole pairs can be hampered in the synthesized composite. Due to the inhibition of electro-hole pair recombination, the number of holes participating in response to oxidation increases. Subsequently, photogenerated electrons and holes can react with the O_2 and OH^- existence in water to generate superoxide radical anions ($^{\cdot}O_2^-$) and hydroxyl radicals ($^{\cdot}OH$), respectively, for the decomposition of organic dye.

3.6. Identification of degradation fragments during MG and MO mineralization process

In order to confirm formation, the decolourisation of dyes was established the UV–visible spectral with respect to time. The sharp decrease in absorption peaks was observed for both MO (465 nm) and MG (615 nm) with respect to time. The reduction in absorption peaks indicated the decolourisation on selected dyes (Fig. 8a and b).

Moreover, during HPLC analysis, peaks at retention time 8 min (MO) and 7 min (MG) decreased with an increase in reaction time. However, during initial degradation time, a bundle of peaks emerged between retention times 2–4 min and eventually dissipated after 240 min, it revealing the formation of reaction intermediate during degradation process (Fig. 8c and d). The GC–MS analysis was performed for MG and MO after 70 and 140 min of photocatalysis of selected dyes under visible light. For MG degradation, different fragments were observed at m/z ratios of 332 (A), 211 (B), 227 (C), 122 (D) and 131 (E). During degradation first step involves Cl^- removal from MG to form fragment with m/z 316. The $^{\cdot}OH$ radical attack resulted in the demethylation with formation of fragment A (m/z, 332). The attack of $^{\cdot}OH$ radicals on central carbon atom and demethylation results in the formation of a fragment with m/z ratio 332 and 302. Moreover, the fragments B (m/z, 211), C (m/z, 227) and D (m/z, 172) were formed by demethylation, nitration and oxidation process. Lastly, these fragments were mineralized into CO_2 and H_2O. The obtained degradation fragments were also on accordance with previous work reported (Ghaedi et al., 2015, Ai et al., 2010). The GCMS analysis of degraded MO shows fragments F, G, H and I were observed with m/z 320, 306, 322 and 308, respectively. The fragment F was formed by the demethylation of MO dye (Fig. 8e and f). During photocatalysis, OH radical attack mainly caused the formation of fragments with m/z ratio, G, H and I (Yong et al., 2015). The results of GCMS and HPLC demonstrated that no toxic intermediates were identified during the photodegradation process, whereas the complete mineralization of organic dyes MG and MO in carbon dioxide (CO_2) and water (H_2O) was achieved (Le et al., 2016).

3.7. Magnetic separation and recyclability of ZnO/ZF/NG and ZnO/CF/NG

In addition to photocatalytic activity, recyclability and separation of photocatalyst are very crucial for heterogeneous photocatalysis. We measured the magnetization hysteresis

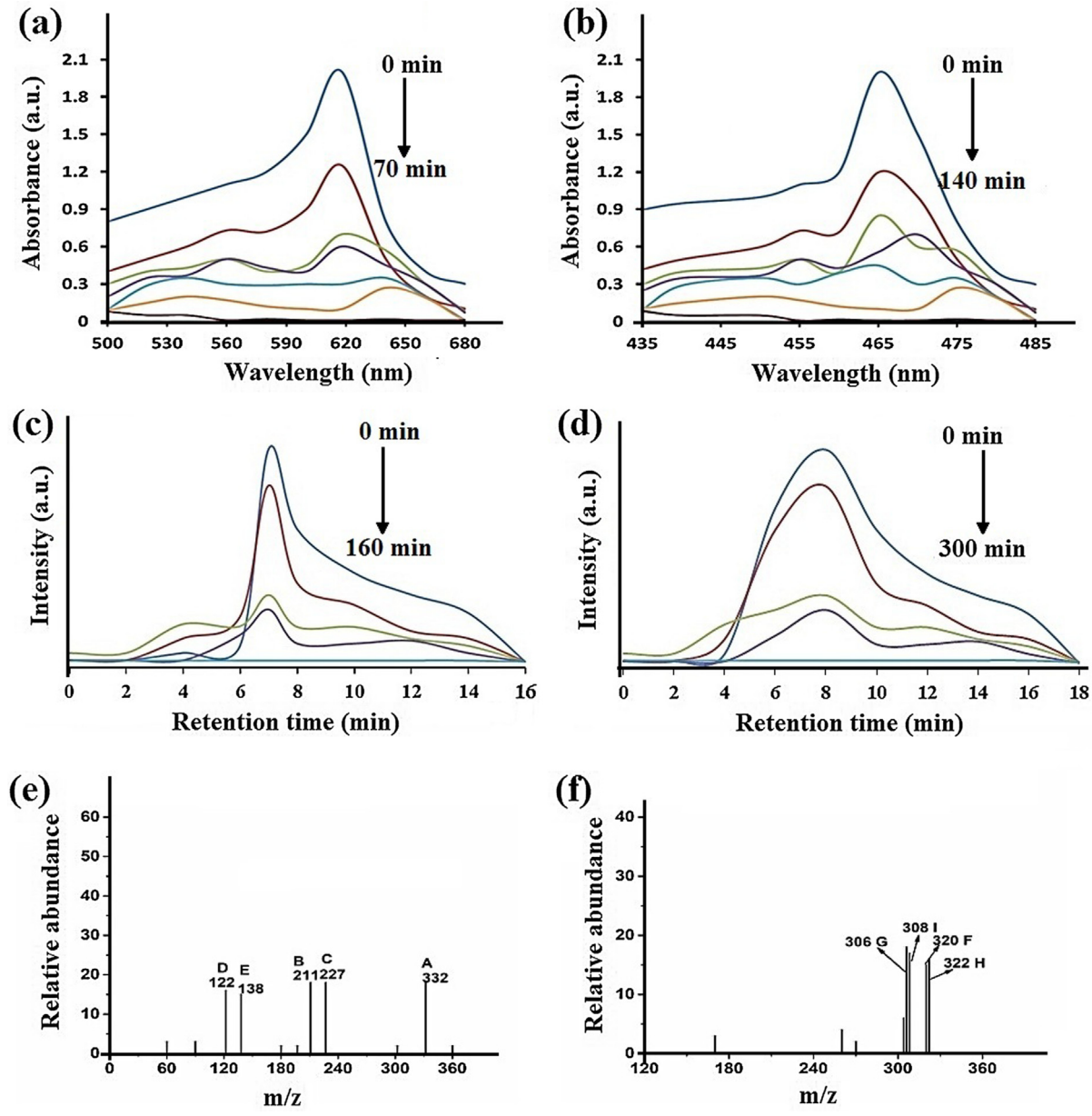

Fig. 8 UV–visible spectra of ZnO/ZF/NG showing degradation of (a) MG and (b) MO during degradation process using HPLC profile of (c) MG and (d) MO during mineralization process, GC–MS analysis of (e) MG after 70 min and (f) MO after 150 min. Reaction conditions: [MO] = 1.5×10^{-5} mol dm^{-3}; [MG] = 1×10^{-5} mol dm^{-3}; [catalyst] = 50 mg/100 mL; pH = 4.0(MO); 6 (MG); reaction time = 70 min (MG) and 140 min (MO), Light Intensity = 750 lx.

loops at room temperature which are shown in Fig. 9a and c. ZnO/ZF/NG displayed superparamagnetic behavior and was isolated from the reaction solution in 20 s using an external magnetic field (Fig. 9b). The saturation magnetization (M_s) and were found to be 55 emu g^{-1}. The coercivity (H_c) for ZnO/ZF/NG was zero (Fig. 9a). The magnetization hysteresis curve of ZnO/CF/NG reveals a typical ferromagnetic nature having saturation magnetization (Ms) value of about 34 emu g^{-1} and coercivity (H_c) value of about 12,580 Oe (Fig. 9c). ZnO/CF/NG was magnetically isolated from the solution phase in 2 min under external magnetic field (Fig. 9d). During recycle experiments, photocatalysts were magnetically separated and used for next consecutive cycle. Both ZnO/CF/NG and ZnO/ZF/NG showed significant recycling performance for ten catalytic cycles. After ten cycles, ZnO/ZF/NG had 79% and 80% of removal efficiency for MG and MO degradation, respectively. While 85 and 82% of MG and MO were photodegraded after ten cycles using ZnO/ZF/NG photocatalyst (Fig. 9e and f). The recycle experiments indicated significant stability and recyclability of ZnO/ZF/NG and ZnO/CF/NG photocatalyst for dye degradation. Furthermore, SEM, FTIR and XRD images did not show any significant morphological or chemical changes in ZnO/ZF/NG and ZnO/CF/NG photocatalyst after ten catalytic cycles (Fig. S4). It directed towards the stability of photocatalyst during degradation process.

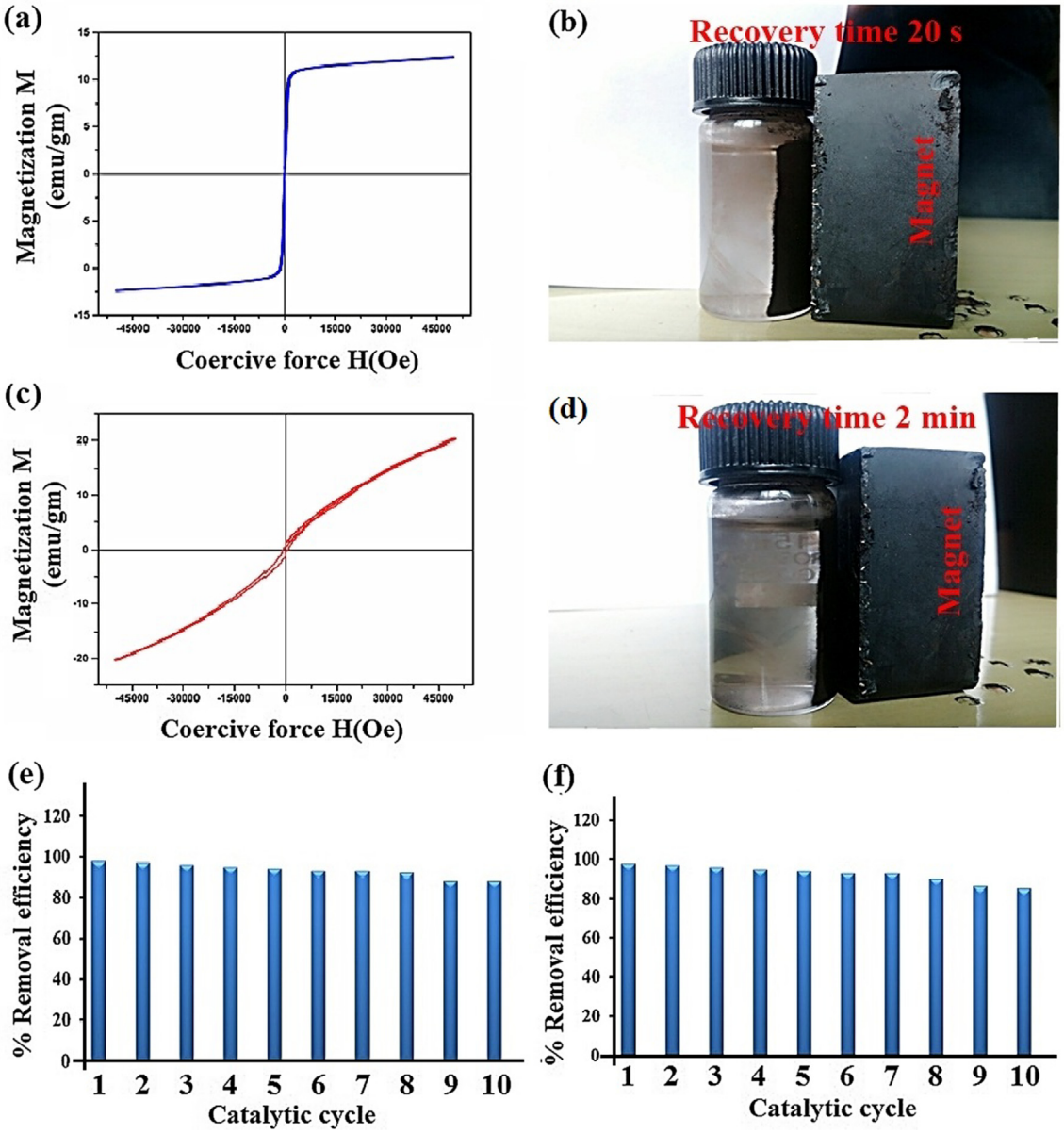

Fig. 9 Hysteresis curve and magnetic separation of ZnO/ZF/NG (a–b), Hysteresis curve and magnetic separation of ZnO/CF/NG (c–d), Recycle efficiency of ZnO/ZF/NG (e) and ZnO/CF/NG (f) for MG removal. Reaction conditions: [MO] = 1.5×10^{-5} mol dm^{-3}; [MG] = 1×10^{-5} mol dm^{-3}; [catalyst] = 50 mg/100 mL; pH = 4.0(MO); 6 (MG); reaction time = 70 min (MG) and 140 min (MO), Light Intensity = 750 lx.

4. Conclusion

In summary, ZnO/ZF/NG and ZnO/CF/NG nanocomposites with enhanced photocatalytic activity were successfully fabricated and characterized. Nitrogen-doped graphene acted as a sink material that eventually led to reduction in charge carrier recombination and increase in photodegradation activity of nanocomposites. ZnO/ZF/NG nanocomposite possessed simple type-II heterojunction whereas ZnO/CF/NG nanocomposite followed z-scheme path for dye degradation and ensued significant diminution in photogenerated electron-hole pair recombination. A proposed mechanistic view of the nanocomposites was given with the generation of radicals that clearly exposed the degradation process of dye. Furthermore, ZnO/ZF/NG and ZnO/CF/NG nanocomposites exhibited higher degradation ability in the exclusion of dyes by generating reactive species such as electrons, holes, superoxides and hydroxyl radicals. Hydroxyl radicals ($OH^{\bullet}$) and holes (h^{+}_{VB}) were the main reactive species responsible for the degradation of dyes. ZnO/ZF/NG and ZnO/CF/NG nanocomposites displayed 99% and 94% removal efficiency for MO degradation respectively, whereas 98% and 92% removal efficiency was observed for MG dye degradation. It was concluded from the results that photodegradation efficiency of ZnO/ZF/NG nanocomposite was higher than ZnO/CF/NG nanocomposite for MO and MG eradication. Both, ZnO/ZF/NG and ZnO/CF/NG

nanocomposites were effortlessly recovered by magnet. On the basis of outcomes of this work, ZnO/ZF/NG and ZnO/CF/NG nanocomposites are expected to be promising as a magnetically mendable visible-light driven photocatalyst for dyes mineralization. Recycling experiments of these ternary heterogeneous photocatalyst in wastewater revealed that there was an negligible diminution in photodegradation ability in successive 10 cycles. Overall, this paper demonstrates systematic design of ZnO/ZF/NG and ZnO/CF/NG heterogeneous visible light driven photocatalyst possess realistic stability that enhances their superior photocatalytic performance, recyclability and applicability for wastewater mitigation.

Appendix A. Supplementary material

Supplementary data to this article can be found online at https://doi.org/10.1016/j.arabjc.2019.08.005.

References

Ai, L., Huang, H., Chen, Z., Wei, X., Jiang, J., 2010. Activated carbon/$CoFe_2O_4$ composites: facile synthesis, magnetic performance and their potential application for the removal of malachite green from water. Chem. Eng. J.156, 243–249.

Akhter, H., Murshed, J., Rashed, M.A., Oshima, Y., Nagao, Y., Rahman, M.M., Asiri, A.M., Hasnat, M.A., Uddin, M.N., Siddiquey, I.A., 2017. Fabrication of hydrazine sensor based on silica-coated Fe_2O_3 magnetic nanoparticles prepared by a rapid microwave irradiation method. J. Alloy Compd. 698, 921–929.

Borgohain, C., Senapati, K.K., Sarma, K.C., Phukan, P., 2012. A facile synthesis of nanocrystalline $CoFe_2O_4$ embedded one-dimensional ZnO hetero-structure and its use in photocatalysis. J. Mol. Catal. A-Chem. 363, 495–500.

Chang, J.Q., Zhong, Y., Hu, C.H., Luo, J.L., Wang, P.G., 2019. Study on highly efficient BiOCl/ZnO pn heterojunction: Synthesis, characterization and visible-light-excited photocatalytic activity. J. Mol. Struct. 1183, 209–216.

Chen, L., Ma, W., Dai, J., Zhao, J., Li, C., Yan, Y., 2016. Facile synthesis of highly efficient graphitic-C_3N_4/$ZnFe_2O_4$ heterostructures enhanced visible-light photocatalysis for spiramycin degradation. J. Photochem. Photobiol. A 328, 24–32.

Chen, Q., Wang, Y., Zheng, M., Fang, H., Meng, X., 2018. Nanostructures confined self-assembled in biomimetic nanochannels for enhancing the sensitivity of biological molecules response. J. Mater. Sci. – Mater. El. 29, 19757–19767.

Dutta, V., Singh, P., Shandilya, P., Sharma, S., Raizada, P., Saini, A. K., Gupta, V.K., Hosseini-Bandegharaei, A., Agarwal, S., Rahmani-Sani, A., 2019. Review on advances in photocatalytic water disinfection utilizing graphene and graphene derivatives-based nanocomposites. J. Environ Chem. Eng. 1; 7(3), 103132.

El-Daly, S.A., Rahman, M.M., Alamry, K.A., Asiri, A.M., 2015. Fluorescence quenching of perylene DBPI dye by colloidal low-dimensional gold nanoparticles. J. Fluoresc. 25, 973–978.

Ferdosi, E., Bahiraei, H., Ghanbari, D., 2019. Investigation the photocatalytic activity of $CoFe_2O_4$/ZnO and $CoFe_2O_4$/ZnO/Ag nanocomposites for purification of dye pollutants. Sep. Purif. Technol. 211, 35–39.

Gan, L., Shang, S., Yuen, C.W.M., Jiang, S.X., Hu, E., 2015. Hydrothermal synthesis of magnetic $CoFe_2O_4$/graphene nanocomposites with improved photocatalytic activity. Appl. Surf. Sci. 351, 140–147.

Gautam, S., Shandilya, P., Priya, B., Singh, V.P., Raizada, P., Rai, R., Valente, M.A., Singh, P., 2017. a. Superparamagnetic $MnFe_2O_4$ dispersed over graphitic carbon sand composite and bentonite as magnetically recoverable photocatalyst for antibiotic mineralization. Sep. Purif. Technol. 172, 498–511.

Gautam, S., Shandilya, P., Singh, V.P., Raizada, P., Singh, P., 2016. Solar photocatalytic mineralization of antibiotics using magnetically separable $NiFe_2O_4$ supported onto graphene sand composite and bentonite. J. Water Process Eng. 14, 86–100.

Ghaedi, M., Hajjati, S., Mahmudi, Z., Tyagi, I., Agarwal, S., Maity, A., Gupta, V.K., 2015. Modeling of competitive ultrasonic assisted removal of the dyes–Methylene blue and Safranin-O using Fe_3O_4 nanoparticles. Chem. Eng. J. 268, 28–37.

Gu, J., Jin, Y., Zhou, Y., Zhang, M., Wu, Y., Wang, J., 2013. Unseeded organotemplate-free hydrothermal synthesis of heteroatomic MFI zeolite poly-nanocrystallites. J. Mater. Chem. A. 1, 2453–2460.

Guo, H.L., Su, P., Kang, X., Ning, S.K., 2013. Synthesis and characterization of nitrogen-doped graphene hydrogels by hydrothermal route with urea as reducing-doping agents. J. Mater. Chem. A. 1 (6), 2248–2255.

Guo, X., Fu, Y., Hong, D., Yu, B., He, H., Wang, Q., Xing, L., Xue, X., 2016. High-efficiency sono-solar-induced degradation of organic dye by the piezophototronic/photocatalytic coupling effect of FeS/ZnO nanoarrays. Nanotechnology 27, 375704.

Guo, X., Zhu, H., Li, Q., 2014. Visible-light-driven photocatalytic properties of ZnO/$ZnFe_2O_4$ core/shell nanocable arrays. Appl. Catal. B – Environ. 160, 408–414.

Gupta, V.K., Pathania, D., Singh, P., 2014. Pectin–cerium (IV) tungstate nanocomposite and its adsorptional activity for removal of methylene blue dye. Int. J. Environ. Sci. Technol. 11, 2015–2024.

Hasija, V., Raizada, P., Sudhaik, A., Sharma, K., Kumar, A., Singh, P., Jonnalagadda, S.B., Thakur, V.K., 2019. Recent advances in noble metal free doped graphitic carbon nitride based nanohybrids for photocatalysis of organic contaminants in water: a review. Appl. Mater. Today 15, 494–524.

Hasnat, M.A., Aoun, S.B., Uddin, S.N., Alam, M.M., Koay, P.P., Amertharaj, S., Rashed, M.A., Rahman, M.M., Mohamed, N., 2014. Copper-immobilized platinum electrocatalyst for the effective reduction of nitrate in a low conductive medium: Mechanism, adsorption thermodynamics and stability. Appl. Catal. A-Gen. 478, 259–266.

He, Y., Zhang, L., Wang, X., Wu, Y., Lin, H., Zhao, L., Weng, W., Wan, H., Fan, M., 2014. Enhanced photodegradation activity of methyl orange over Z-scheme type MoO_3–g-C_3N_4 composite under visible light irradiation. RSC Adv. 4, 13610–13619.

Hegazy, E.Z., Kosa, S.A., Elmaksod, I.H.A., Mojamami, J.T., 2019. Preparation, characterization and photocatalytic evaluation of aluminum doped metal ferrites. Ceram. Int. 45, 7318–7327.

Hong, D., Zang, W., Guo, X., Fu, Y., He, H., Sun, J., Xing, L., Liu, B., Xue, X., 2016. High piezo-photocatalytic efficiency of CuS/ZnO nanowires using both solar and mechanical energy for degrading organic dye. ACS Appl. Mater. Inter. 8, 21302–21314.

Huang, S., Xu, Y., Xie, M., Xu, H., He, M., Xia, J., Huang, Li, Li, H., 2015. Synthesis of magnetic CoFe2O4/g-C3N4 composite and its enhancement of photocatalytic ability under visible-light. Colloids Surf. A 478, 71–80.

Hussain, M.M., Rahman, M.M., Asiri, A.M., 2017. Ultrasensitive and selective 4-aminophenol chemical sensor development based on nickel oxide nanoparticles decorated carbon nanotube nanocomposites for green environment. J. Environ. Sci. 53, 27–38.

Jamwal, D., Kaur, G., Raizada, P., Singh, P., Pathak, D., Thakur, P., 2015. Twin-tail surfactant peculiarity in superficial fabrication of semiconductor quantum dots: toward structural, optical, and electrical features. J. Phys. Chem. C 119, 5062–5073.

Jiang, T., Wang, Y., Meng, D., Wu, X., Wang, J., Chen, J., 2014. Controllable fabrication of CuO nanostructure by hydrothermal method and its properties. Appl. Surf. Sci. 311, 602–608.

Jiang, Y., Chowdhury, S., Balasubramanian, R., 2017. Nitrogen-doped graphene hydrogels as potential adsorbents and photocatalysts for environmental remediation. Chem. Eng. J. 327, 751–763.

Jing, L., Xu, Y., Huang, S., Xie, M., He, M., Xu, H., Li, H., Zhang, Q., 2016. Novel magnetic $CoFe_2O_4/Ag/Ag_3VO_4$ composites: highly efficient visible light photocatalytic and antibacterial activity. Appl. Catal. B-Environ. 199, 11–22.

Kachi, W., Al-Shammari, A.M., Zainal, I.G., 2019. Cobalt Ferrite Nanoparticles: preparation, characterization and salinized with 3-aminopropyl triethoxysilane. Energy Proc. 157, 1353–1365.

Kamranifar, M., Allahresani, A., Naghizadeh, A., 2019. Synthesis and characterizations of a novel $CoFe_2O_4$@ CuS magnetic nanocomposite and investigation of its efficiency for photocatalytic degradation of penicillin G antibiotic in simulated wastewater. J. Hazard. Mater. 366, 545–555.

Kavitha, R., Kumar, S.G., 2019. A review on plasmonic Au-ZnO heterojunction photocatalysts: Preparation, modifications and related charge carrier dynamics. Mater. Sci. Semicond. Process. 93, 59–91.

Le, T.X., Van Nguyen, T., Yacouba, Z.A., Zoungrana, L., Avril, F., Petit, E., Mendret, J., Bonniol, V., Bechelany, M., Lacour, S., Lesage, G., 2016. Toxicity removal assessments related to degradation pathways of azo dyes: toward an optimization of electro-Fenton treatment. Chemosphere 161, 308–318.

Li, C.J., Wang, J.N., Wang, B., Gong, J.R., Lin, Z., 2012. A novel magnetically separable $TiO_2/CoFe_2O_4$ nanofiber with high photocatalytic activity under UV–vis light. Mater. Res. Bull. 47, 333–337.

Liu, Y., Yu, J., Lai, P.T., 2014. Investigation of WO_3/ZnO thin-film heterojunction-based Schottky diodes for H_2 gas sensing. Int. J. Hydrogen Energy 39, 10313–10319.

Lu, X., Yang, L., Bian, X., Chao, D., Wang, C., 2014. Rapid, microwave assisted, and one pot synthesis of magnetic palladium–$CoFe_2O_4$–graphene composite nanosheets and their applications as recyclable catalysts. Part. Part. Syst. Char. 31, 245–251.

Mou, Z., Chen, X., Du, Y., Wang, X., Yang, P., Wang, S., 2011. Forming mechanism of nitrogen doped graphene prepared by thermal solid-state reaction of graphite oxide and urea. Appl. Surf. Sci. 258 (5), 1704–1710.

Nada, A.A., Nasr, M., Viter, R., Miele, P., Roualdes, S., Bechelany, M., 2017. Mesoporous $ZnFe_2O_4$@ TiO_2 nanofibers prepared by electrospinning coupled to PECVD as highly performing photocatalytic materials. J. Phys. Chem. C. 121, 24669–24677.

Nasr, M., Balme, S., Eid, C., Habchi, R., Miele, P., Bechelany, M., 2016. Enhanced visible-light photocatalytic performance of electrospun rGO/TiO_2 composite nanofibers. J. Phys. Chem. C. 121, 261–269.

Nasr, M., Eid, C., Habchi, R., Miele, P., Bechelany, M., 2018. Recent progress on titanium dioxide nanomaterials for photocatalytic applications. Chem. Sus. Chem. 11, 3023–3047.

Pare, B., Jonnalagadda, S.B., Tomar, H., Singh, P., Bhagwat, V.W., 2008. ZnO assisted photocatalytic degradation of acridine orange in aqueous solution using visible irradiation. Desalination 232, 80–90.

Pare, B., Singh, P., Jonnalgadda, S.B., 2009. Artificial light assisted photocatalytic degradation of lissamine fast yellow dye in ZnO suspension in a slurry batch reactor. Indian J. Chem.-A 48, 1364–1369.

Prado, A.G., Costa, L.L., 2009. Photocatalytic decouloration of malachite green dye by application of TiO_2 nanotubes. J. Hazard. Mater. 169, 297–301.

Priya, B., Shandilya, P., Raizada, P., Thakur, P., Singh, N., Singh, P., 2016. Photocatalytic mineralization and degradation kinetics of ampicillin and oxytetracycline antibiotics using graphene sand composite and chitosan supported BiOCl. J. Mol. Catal. A-Chem. 423, 400–413.

Qin, R., Meng, F., Khan, M.W., Yu, B., Li, H., Fan, Z., Gong, J., 2019. Fabrication and enhanced photocatalytic property of TiO_2-ZnO composite photocatalysts. Mat. Lett. 240, 84–87.

Rahman, M.M., Abu-Zied, B.M., Asiri, A.M., 2018. Cu-loaded ZSM-5 zeolites: An ultra-sensitive phenolic sensor development for environmental safety. J. Ind. Eng. Chem. 61, 304–313.

Rahman, M.M., Abu-Zied, B.M., Hasan, M.M., Asiri, A.M., Hasnat, M.A., 2016. Fabrication of a selective 4-amino phenol sensor based on H-ZSM-5 zeolites deposited silver electrodes. RSC Adv. 6, 48435–48444.

Rahman, M.M., Alam, M.M., Asiri, A.M., Islam, M.A., 2017a. Fabrication of selective chemical sensor with ternary $ZnO/SnO_2/Yb_2O_3$ nanoparticles. Talanta 170, 215–223.

Rahman, M.M., Alfonso, V.G., Fabregat-Santiago, F., Bisquert, J., Asiri, A.M., Alshehri, A.A., Albar, H.A., 2017b. Hydrazine sensors development based on a glassy carbon electrode modified with a nanostructured TiO_2 films by electrochemical approach. Microchim. Acta 184, 2123–2129.

Rahman, M.M., Asiri, A.M., 2015. Fabrication of highly sensitive ethanol sensor based on doped nanostructure materials using tiny chips. RSC Adv. 5, 63252–63263.

Raizada, P., Kumari, J., Shandilya, P., Singh, P., 2017. Kinetics of photocatalytic mineralization of oxytetracycline and ampicillin using activated carbon supported ZnO/ZnWO. Desalin. Water Treat. 79, 204–213.

Raizada, Priya, B., Thakur, P., Singh, P., 2016. Solar light induced photodegradation of oxytetracycline using Zr doped TiO_2/CaO based nanocomposite, Indian. J. Chem. 55, 803–809.

Raizada, P., Singh, P., Kumar, A., Pare, B., Jonnalagadda, S.B., 2014a. Zero valent iron-brick grain nanocomposite for enhanced solar-Fenton removal of malachite green. Sep. Purif. Technol. 133, 429–437.

Raizada, P., Singh, P., Kumar, A., Sharma, G., Pare, B., Jonnalagadda, S.B., Thakur, P., 2014b. Solar photocatalytic activity of nano-ZnO supported on activated carbon or brick grain particles: role of adsorption in dye degradation. Appl. Catal. A. 486, 159–169.

Raizada, P., Sudhaik, A., Shandilya, P., Saini, A., Gupta, V., Singh, P., 2019. Fabrication of Ag_3VO_4 decorated phosphorus and sulphur co-doped graphitic carbon nitride as high-dispersed photocatalyst for phenol mineralization and E.Coli disinfection. Sep. Purif. Technol. 212, 887–900.

Sathishkumar, P., Pugazhenthiran, N., Mangalaraja, R.V., Asiri, A. M., Anandan, S., 2013. ZnO supported $CoFe_2O_4$ nanophotocatalysts for the mineralization of Direct Blue 71 in aqueous environments. J. Hazard. Mater. 252, 171–179.

Shandilya, P., Mittal, D., Soni, M., Raizada, P., Hosseini-Bandegharaei, A., Saini, A.K., Singh, P., 2018a. Fabrication of fluorine doped graphene and $SmVO_4$ based dispersed and adsorptive photocatalyst for abatement of phenolic compounds from water and bacterial disinfection. J. Clean. Prod. 203, 386–399.

Shandilya, P., Mittal, D., Soni, M., Raizada, P., Lim, J.H., Jeong, D. Y., Dewedi, R.P., Saini, A.K., Singh, P., 2018b. Islanding of $EuVO_4$ on high-dispersed fluorine doped few layered graphene sheets for efficient photocatalytic mineralization of phenolic compounds and bacterial disinfection. J. Taiwan Inst. Chem. Eng. 93, 528–542.

Shandilya, P., Mittal, D., Sudhaik, A., Soni, M., Raizada, P., Saini, A. K., Singh, P., 2019. $GdVO_4$ modified fluorine doped graphene nanosheets as dispersed photocatalyst for mitigation of phenolic compounds in aqueous environment and bacterial disinfection. Sep. Purif. Technol. 210, 804–816.

Sharma, K., Dutta, V., Sharma, S., Raizada, P., Hosseini-Bandegharaei, A., Thakur, P., Singh, P., 2019. Recent advances in enhanced photocatalytic activity of bismuth oxyhalides for efficient photocatalysis of organic pollutants in water: a review. J. Ind. Eng. Chem. 75 (28), 1–20.

Singh, P., Gautam, S., Shandilya, P., Priya, B., Singh, V.P., Raizada, P., 2017a. Graphene bentonite supported $ZnFe_2O_4$ as superparamagnetic photocatalyst for antibiotic degradation. Adv. Mater. Lett. 8, 229–238.

Singh, P., Priya, B., Shandilya, P., Raizada, P., Singh, N., Pare, B., Jonnalagadda, S.B., 2019a. Photocatalytic mineralization of antibiotics using 60% WO3/BiOCl stacked to graphene sand composite and chitosan. Arab. J. Chem. 12, 4627–4645. https://doi.org/10.1016/j.arabjc.2016.08.005.

Singh, P., Raizada, P., Pathania, D., Kumar, A., Thakur, P., 2013. Preparation of BSA-ZnWO4 nanocomposites with enhanced adsorptional photocatalytic activity for methylene blue degradation. Int. J. Photoenergy 2013, 7. https://doi.org/10.1155/2013/726250.

Singh, P., Raizada, P., Sudhaik, A., Shandilya, P., Thakur, P., Agarwal, S., Gupta, V.K., 2019b. Enhanced photocatalytic activity and stability of AgBr/BiOBr/graphene heterojunction for phenol degradation under visible light. J. Saudi Chem. Soc. 23 (5), 586–599.

Singh, P., Shandilya, P., Raizada, P., Sudhaik, A., Rahmani-Sani, A., Hosseini-Bandegharaei, A., 2020. Review on various strategies for enhancing photocatalytic activity of graphene based nanocomposites for water purification. Arab. J. Chem. 13, 3498–3520. https://doi.org/10.1016/j.arabjc.2018.12.001.

Singh, R., Ladol, J., Khajuria, H., Sheikh, H.N., 2017b. Nitrogen doped graphene nickel ferrite magnetic photocatalyst for the visible light degradation of methylene blue. Acta Chim. Slov. 64, 170–178.

Sharma, S., Pathania, D., Singh, P., 2013. Preparation, characterization and Cr(VI) adsorption behavior study of poly(acrylic acid) grafted Ficus carica bast fiber. Adv. Mat. Lett. 4 (4), 271–276.

Sudhaik, A., Raizada, P., Shandilya, P., Jeong, D.Y., Lim, J.H., Singh, P., 2018a. Review on fabrication of graphitic carbon nitride based efficient nanocomposites for photodegradation of aqueous phase organic pollutants. J. Ind. Eng. Chem. 67, 28–51.

Sudhaik, A., Raizada, P., Shandilya, P., Singh, P., 2018b. Magnetically recoverable graphitic carbon nitride and $NiFe_2O_4$ based magnetic photocatalyst for degradation of oxytetracycline antibiotic in simulated wastewater under solar light. J. Environ. Chem. Eng. 6, 3874–3883.

Valtchev, V., Majano, G., Mintova, S., Pérez-Ramírez, J., 2013. Tailored crystalline microporous materials by post-synthesis modification. Chem. Soc. Rev. 42, 263–290.

Wang, C., Tan, X., Yan, J., Chai, B., Li, J., Chen, S., 2017. Electrospinning direct synthesis of magnetic $ZnFe_2O_4$/ZnO multiporous nanotubes with enhanced photocatalytic activity. Appl. Surf. Sci. 396, 780–790.

Wang, Y., Jiang, T., Meng, D., Yang, J., Li, Y., Ma, Q., Han, J., 2014. Fabrication of nanostructured CuO films by electrodeposition and their photocatalytic properties. Appl. Surf. Sci. 317, 414–421.

Xue, X., Zang, W., Deng, P., Wang, Q., Xing, L., Zhang, Y., Wang, Z. L., 2015. Piezo-potential enhanced photocatalytic degradation of organic dye using ZnO nanowires. Nano Energy 13, 414–422.

Yamamoto, A., Mizuno, Y., Teramura, K., Shishido, T., Tanaka, T., 2013. Effects of reaction temperature on the photocatalytic activity of photo-SCR of NO with NH_3 over a TiO_2 photocatalyst. Catal. Sci. Technol. 3, 1771–1775.

Yao, L., Deng, H., Huang, Q.A., Su, Q., Du, G., 2017. Three-dimensional carbon-coated $ZnFe_2O_4$ nanospheres/nitrogen-doped graphene aerogels as anode for lithium-ion batteries. Ceram. Int. 43, 1022–1028.

Yong, L., Zhanqi, G., Yuefei, J., Xiaobin, H., Cheng, S., Shaogui, Y., Lianhong, W., Qingeng, W., Die, F., 2015. Photodegradation of malachite green under simulated and natural irradiation: kinetics, products, and pathways. J. Hazard. Mater. 285, 127–136.

Yuan, E., Wu, G., Dai, W., Guan, N., Li, L., 2017. One-pot construction of Fe/ZSM-5 zeolites for the selective catalytic reduction of nitrogen oxides by ammonia. Catal. Sci. Technol. 7, 3036–3044.

Zamiri, R., Salehizadeh, S.A., Ahangar, H.A., Shabani, M., Rebelo, A., Kumar, J.S., Soares, M.J., Valente, M.A., Ferreira, J.M.F., 2017. Optical and magnetic properties of ZnO/$ZnFe_2O_4$ nanocomposite. Mater. Chem. Phys. 192, 330–338.

Zarrabi, M., Haghighi, M., Alizadeh, R., Mahboob, S., 2019. Solar-light-driven photodegradation of organic dyes on sono-dispersed ZnO nanoparticles over graphene oxide: Sono vs. conventional catalyst design. Sep. Purif. Technol. 211, 738–752.

Zhang, Z.L., Wan, M., Mao, Y.L., 2012. Enhanced photovoltaic effect of TiO_2-based composite $ZnFe_2O_4$/TiO_2. J. Photochem. Photobiol. A 233, 15–19.

Zhu, H.Y., Jiang, R., Fu, Y.Q., Li, R.R., Yao, J., Jiang, S.T., 2016. Novel multifunctional $NiFe_2O_4$/ZnO hybrids for dye removal by adsorption, photocatalysis and magnetic separation. Appl. Surf. Sci. 369, 1–10.